Contributions to Mineralogy and Petrology (2026) 181:31
https://doi.org/10.1007/s00410-026-02318-9

ORIGINAL PAPER

Geometry controls on the structure and geochemistry of olivine low-angle grain boundaries

Dimitrios Dimitriou[1] · Steven M. Reddy[1,2] · Denis Fougerouse[1,2] · David W. Saxey[2] · Katy Evans[1] · Tommaso Tacchetto[1,3] · Katharina Marquardt[4,5]

Received: 7 November 2025 / Accepted: 22 March 2026

Abstract

Olivine low-angle grain boundaries (LAGBs) influence the upper mantle properties, but the role of geometry in their structure and chemical composition remains largely unexplored. Here, we characterise and compare three tilt LAGBs with a 4.5° misorientation angle but different misorientation axes in a mantle xenolith. Electron backscatter diffraction (EBSD) was used to characterise three olivine grains, containing one LAGB aligning with the (001)[100] slip system, and two LAGBs with (010)[100] slip. Within the (010)[100] LAGBs, transmission electron microscopy (TEM) shows dislocation cores regularly spaced at 5.8 nm. Direct dislocations imaging in the (001)[100] LAGB was hindered by lamella orientation. Atom probe tomography (APT) reveals segregation of Al, Ca, Fe, H and Ti to the LAGBs, accompanied by Mg depletion. In the (010)[100] LAGBs, the segregated elements are concentrated in linear arrays (~5.8 nm spacing), consistent with segregation to dislocations. In the (001)[100] LAGBs, although segregated elements appear evenly distributed, 2D profiles show regularly spaced features at ~4.8 nm along the boundary, indicative of dislocation spacing. Interfacial excess calculations reveal differences in elemental segregation between boundaries. The (001)[100] LAGB has greater H segregation, while the LAGB in the seemingly smaller grain exhibits decreased Al, Ca and Fe enrichment. These findings suggest that LAGB geometry influences elemental segregation. Because these geometries are associated with specific mantle fabrics, the segregation patterns may influence differences in phase transitions, creep behaviour, electrical conductivity, and seismic properties in the upper mantle.

Keywords Olivine · Grain boundaries · Slip system · Dislocations · Transmission electron microscopy · Atom probe tomography

Introduction

Olivine grain boundaries are important microstructures largely affecting the properties of the mantle. Studies of olivine high-angle grain boundaries (HAGBs) show that diffusion along them is several orders of magnitude faster than volume diffusion (Dohmen and Milke 2010; Wagner et al. 2016), with implications for metamorphic processes (e.g. acting as fluid transport pathways) (Putnis and John 2010). They are also a reservoir of incompatible trace elements (Hiraga et al. 2002; 2004; Tacchetto et al. 2021) and, particularly hydrogen (Sommer et al. 2008; Demouchy 2010b; Tacchetto et al. 2021), which has significant effects on the rheological properties of the mantle, acting as a weakening agent and accelerating grain boundary sliding (Katayama and Karato 2008; Faul et al. 2016).

Communicated by Ralf Dohmen.

✉ Dimitrios Dimitriou
dimitrios.dimitriou@curtin.edu.au

1 School of Earth and Planetary Sciences, Curtin University, Bentley, WA 6102, Australia

2 Geoscience Atom Probe Facility, John de Laeter Centre, Curtin University, Bentley, WA 6102, Australia

3 CSIRO Mineral Resources, Waterford, WA 6152, Australia

4 Department of Materials, Royal School of Mines, Imperial College London, London SW7 2AZ, UK

5 Department of Materials, University of Oxford, Oxford, Oxfordshire OX1 3PH, UK

Published online: 10 April 2026

Experimental studies in olivine have shown that dislocation slip occurs along a limited combination of slip directions along specific planes, called slip systems (Katayama et al. 2004; Mainprice et al. 2005; Raterron et al. 2007). Specific slip systems are, in most cases, dominant in specific olivine fabrics. These slip systems and associated fabrics are shown in Table 1. Studies have also defined relationships between specific dislocation slip in olivine and hydrogen content (Katayama et al. 2004; Jung et al. 2006; Skemer and Hansen 2016). For example, (100)[001] slip system (most dominant in C-type fabric) is commonly associated with the highest hydrogen content. Conversely, (010)[100] slip system (dominant in A-type fabric) is described as the least hydrous.

Grain boundaries are discrete planar features that mark the interfaces between two adjacent grains of the same mineral. They are associated with a change in crystallographic orientation and, depending on their misorientation angle, they are separated in low-angle grain boundaries (LAGBs) and high-angle grain boundary (HAGBs), with the threshold between them being different for different materials. LAGBs consist of systematic arrays of dislocations where the number and density of dislocations increase with misorientation angle. When the boundary can no longer be described by this dislocation model, the interface is referred to as a HAGB. For olivine this transition has been set at 22° of misorientation (Heinemann et al. 2005), although the transition could be as large as 32° (Adjaoud et al. 2012).

A grain boundary is defined by five independent macroscopic degrees of freedom (parameters) in orientation space (Lloyd et al. 1997; Marquardt and Faul 2018). Three of these parameters describe the misorientation of the crystal lattice between the adjacent grains. Misorientation is the necessary rotation to bring the two crystal frames of the grains in coincidence. The disorientation angle describes the misorientation with the smallest unique rotation to bring the grains in coincidence. Two parameters describe the misorientation axis (also called rotation axis), around which the rotation happens. The other two parameters are used to describe the grain boundary plane, by describing the axis that is normal to the plane. It is worth mentioning here that disorientation angle and misorientation angle, while related, are not the same, with disorientation angle describing the minimum rotation required, while misorientation includes any equivalent rotations allowed by crystal symmetry that would bring the two crystal lattices into coincidence. Here the term disorientation angle is used, as it corresponds to the acquired data, but the term misorientation is used when describing the rotation axis combined with the rotation angle.

Table 1 Olivine slip systems and the fabrics they are most commonly associated with

Slip Plane	Slip Direction	Olivine fabric
(010)	[100]	A-type
(010)	[001]	B-type
(001)	[001]	C-type
{011}	[100]	D-type
(001)	[100]	E-type

The study of olivine grain boundaries has been the focus of many works, but their geometric and geochemical complexity in combination with their nm-sized width have left many of their aspects yet unexplored. Most studies of grain boundary structures have been done on experimentally deformed olivine using transmission electron microscopy (TEM) and electron back-scatter diffraction microscopy (EBSD) (e.g. Bollinger et al. 2019; Ferreira et al. 2021; Hiraga et al. 2002; Marquardt and Faul 2018). Olivine grain boundaries associated H in has been reported through TEM, although these observations are indirect and fail to quantify the concentration of H (Khisina and Wirth 2002; Hiraga et al. 2004; Khisina et al. 2008). Other studies reporting H in grain boundaries are with the use of TEM and Fourier-transform Infrared Spectroscopy (FTIR) (Kitamura et al. 1987; Hermann et al. 2007; Sommer et al. 2008; Demouchy 2010b), but FTIR lacks the nanometre- scale resolution required to target the grain boundaries. Moreover, these studies have mainly focused on HAGBs, leaving a knowledge gap in the structure and chemistry of LAGBs and their effect on rock properties.

Some limitations in the study of grain boundaries have recently been overcome through correlative EBSD crystallographic analysis and Atom Probe Tomography (APT) high spatial resolution geochemical analysis. APT enables quantitative compositional analyses at nanometre-scale resolution and provides 3D visualisation of the distribution of atoms in mineral grain boundaries (Cukjati et al. 2019; Fougerouse et al. 2019, 2021; Montalvo et al. 2019; Piazolo et al. 2016; Reddy et al. 2020 and references therein). APT analyses of olivine grain boundaries have revealed the significance of disorientation angle and showed a positive correlation between trace element segregation and disorientation angle (Tacchetto et al. 2021). Here we investigate the relationship between minor (Fe, Ca and Al) and trace element (Ti and H) segregation and grain boundary type by correlating EBSD, TEM and APT for selected olivine LAGBs. The results allow to complete another piece of puzzle in the interpretation of the complex grain boundary variables providing a better understanding on the response that nanoscale heterogeneities might have on the macroscopic response of polycrystalline aggregates, in particular with potential implications for upper mantle properties.

Geological setting and sample

Sardinia and parts of Corsica belong to a micro-plate that broke apart from southern Europe during Late Eocene-Early Oligocene (Lustrino et al. 2004; 2007). The plate is located between the Tyrrhenian and the Ligurian-Provencal extensional basins (Peccerillo 2017). Two distinct volcanic cycles are seen on the island of Sardinia. The first Oligocene–Miocene volcanic cycle is orogenic and is linked to the counterclockwise rotation of the micro-plate and the subduction of the Ionian Tethys (Carminati et al. 2010; Lustrino et al. 2013). The second anorogenic volcanic cycle took place in the late Miocene-Quaternary (Lustrino et al. 2000, 2007; Rocco et al. 2012). This volcanic cycle has been linked to the opening of the Tyrrhenian basin and the associated mantle upwelling (Peccerillo 2017) (Fig. 1).

The sample investigated is a mantle xenolith found in mafic alkaline lavas from the second cycle of volcanism. Specifically, it comes from the 3.8–2.1 Ma Gerrei volcanic field which consists of hawaiite and basaltic andesite-type lavas (Peccerillo 2017; Rocco et al. 2012). The xenolith is lherzolitic, and it is interpreted to represent mantle material captured from an active subduction zone (Rocco et al. 2012). It is characterised by a coarse-granular texture, with a modal composition of 59% olivine, 26% orthopyroxene, 11% clinopyroxene and 7% spinel. Its equilibrium temperature was calculated at 1000 °C and its oxygen fugacity at 0.17 (Rocco et al. 2012). Petrography, composition, geochemical analyses, equilibration temperature and oxygen fugacity of the sample indicate that the xenolith has undergone partial melting and subsequent re-fertilisation by alkaline metasomatism before incorporation into the host lava (Rocco et al. 2012).

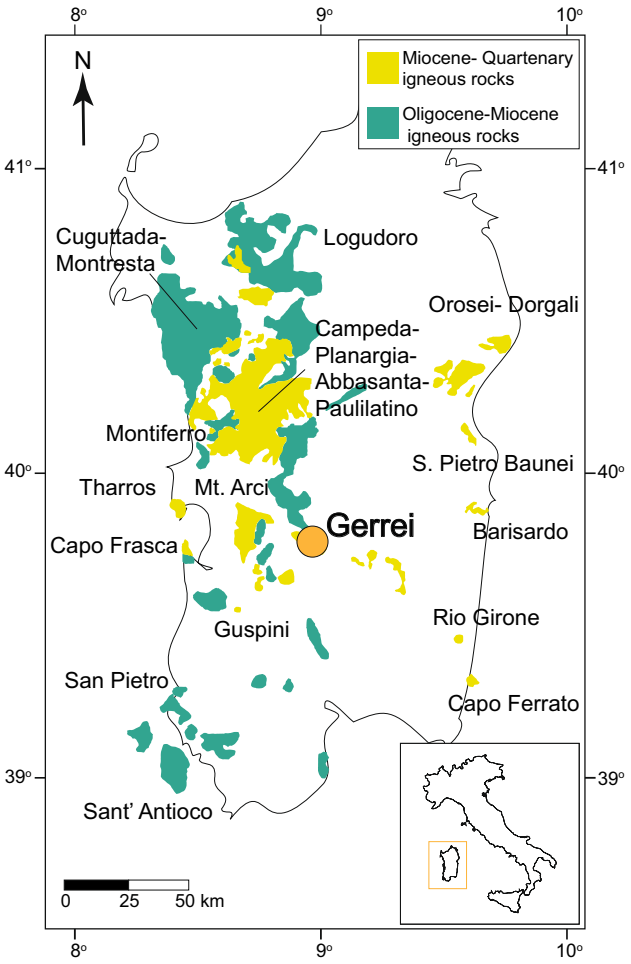

Fig. 1 Simplified map showing the lava localities of the two Cenozoic volcanism cycles in Sardinia. The star denotes the lava containing the mantle xenolith sample investigated in this work (modified from Rocco et al. 2012)

Methods

Secondary electron (SE), backscatter electron (BSE) and electron backscatter diffraction (EBSD) data were collected using a Tescan CLARA field emission microscope (FE-SEM) at the John de Laeter Centre at Curtin University, Perth, Australia. An acceleration voltage of 20 kV and beam current of 1nA were used for data acquisition. The EBSD patterns were collected using an Oxford Instruments Symmetry detector and Aztec Synergy software (v5.1), using a stage tilt of 70° and a working distance of 20 mm. Two large area EBSD maps were collected at step sizes of 5 µm and 3.5 µm to locate olivine grains with LAGBs. Olivine electron backscatter patterns were indexed using parameters from Miyake et al. (1987) with lattice spacings of a = 4.76 Å, b = 10.22 Å, and c = 5.98 Å in the space group Pbnm. AZtecCrystal software v2.1 was used for the post-acquisition processing of the data. Single, misindexed pixels were removed, followed by a five-neighbour zero solution correction. The latter assigns neighbour pixel phase and orientation to non-indexed pixels, as long as at least five of the surrounding pixels are indexed. A minor systematic misindexing associated with 60° around [100] was corrected using the pseudosymettry function of Aztec Crystal. Lastly, a Kuwahara filter (quadrant type with a three-pixel radius) was applied to reduce angular noise further and improve map quality (Humphreys et al. 2001).

Single olivine grains were defined using the previously reported critical disorientation angle of 22° (Adjaoud et al. 2012; Marquardt et al. 2015). LAGBs in olivine grains were examined to identify three LAGBs with a disorientation angle of 4.5° ± 0.5° and different misorientation axes. The latter relate to the operation of different slip systems in olivine. These LAGBs were mapped using EBSD with a step size of at least 1% of the grain size and ranged from 1 to 3 µm. Post-acquisition processing of these detailed EBSD

maps was identical to the post-processing of the large area maps.

Electron-transparent foils for TEM and needle-shaped specimens for APT were prepared from each of the three examined LAGBs using a Tescan Lyra3 Ga^+ Focused Ion Beam Scanning Electron Microscope (FIB-SEM) at the John de Laeter Centre at Curtin University (Fig. S1). Two site-specific TEM foils were made for each of the LAGB following known procedures (Overwijk et al. 1993; Schaffer et al. 2011). APT specimens were created using the site-specific "button" method described by Rickard et al. (2020). The APT specimens were mounted on Si microtip coupons using previously established approaches (Thompson et al. 2007). For both techniques, the FIB was operated at 30 kV. In a final polishing step, the acceleration voltage was decreased to 2 keV to minimize the amorphization layer caused by high-energy implanted Ga + ion implantations.

The thin foils were investigated with TEM and scanning TEM (STEM) using a FEI Talos F200i (S)TEM equipped with an extreme brightness field emission gun (X-FEG) Schottky electron source and a 100 mm^2, 1.28 srad Bruker XFlash 6–100 single area EDS detector at the Department of Material Sciences, at Imperial College, London, United Kingdom. The microscope was operated at 200 kV, and the spot size was varied between 4–11 to control the beam current between STEM, SAD and TEM modes. The instrument was used to collect bright field (BF), high-resolution (HR) TEM and STEM micrographs as well as EDS elemental mapping.

The APT specimens were analysed using a CAMECA LEAP 4000X HR at the Geoscience Atom Probe Facility (John de Laeter Centre, Curtin University). The instrument was operated using a base temperature of 60 K, an ultraviolet laser ($\lambda = 355$ nm) at 150–200 pJ pulse energy, 200 kHz frequency and a detection rate of 0.005–0.008 ions/pulse. The obtained data were processed and reconstructed using the Cameca AP Suite 6 (version 6.1) software. Peaks in the mass-to-charge ratio spectra were ranged when twice higher than the background, and ions were assigned to them. The peaks were ranged in a way that accommodates delayed evaporation events related to peak tails. The H peaks at 1, 2 and 3 Da were not ranged, as they are associated with residual H in the chamber. The AP Suite 6 integrated voltage-evolution reconstruction algorithm was used to reconstruct the 3D position of the atoms in the specimen. The reconstruction of specimens follows the workflow by Dimitriou et al. (2025). A detailed list of acquisition, processing and reconstruction parameters is provided in Table S2 (Blum et al. 2018).

Isoconcentration surfaces were generated using the atomic concentration of Al and Ca with total isoconcentration value of 0.5 at% as the lower limit to identify the LAGBs and their structure. This value was chosen, as it was sufficient to define the LAGBs across all specimens. Spurious, small clusters with the same isoconcentration value not associated with the interfaces were filtered out. The produced isoconcentration surfaces were used as a guide to create a $30 \times 30 \times 30$ nm cube placed perpendicular to the boundary surface, in a representative area of the boundary. 1D-concentration profiles for the atomic concentration of Mg, Si, Al, Ca, Fe, Ti and H were then produced.

Quantification of segregation in LAGBs can be affected by their reconstructed three-dimensional structure, element specific grain boundary effective widths and the intrinsic normalisation of atomic concentration measurements. To overcome this, the 1D-concentration profiles were used as an input in the code by Theska and Primig (2024) to calculate the interfacial excess for each LAGB. In this approach, the Gibbs dividing surface, an idealised boundary placed within the grain boundaries, is calculated as the midpoint point between the global maximum and minimum of the concentration difference (the point of the most abrupt increase and the point of most abrupt decrease). The interfacial excess quantifies the difference of a component between the intragranular region and the calculated dividing surface and is expressed in number of molecules of the respective species per unit area (nm^{-2}) (Felfer et al. 2015).

Finally, 2D profiles were obtained using the concentration of Al. The 2D profiles were visually positioned, to the best of our ability, perpendicular to the direction of the misorientation axes, as determined by EBSD pole figures. The 2D profiles help examine in further detail the structure of LAGBs from the APT data.

Results

Grain boundary microstructural analyses

The olivine LAGBs are geometrically characterised based on the crystallographic orientation patterns and the geometry of the boundary trace to define the misorientation axes of the slip planes and slip directions (Lloyd et al. 1997; 2021; Reddy et al. 2007) (Fig. 2). In the case of LAGB-1, the misorientation axis aligned with the [010] crystallographic direction. There are no possible boundary geometries, constrained by the boundary trace, where the misorientation axis is 90° to the boundary plane, indicating that LAGB-1 cannot be a twist boundary. Instead, if LAGB-1 is a tilt boundary, then the misorientation axis and trace of the boundary can be used to constrain the geometry of the boundary (Fig. 2). For LAGB-1, the slip plane is (001), and the slip direction is parallel to the [100] axis. LAGB-2 and LAGB-3 have a

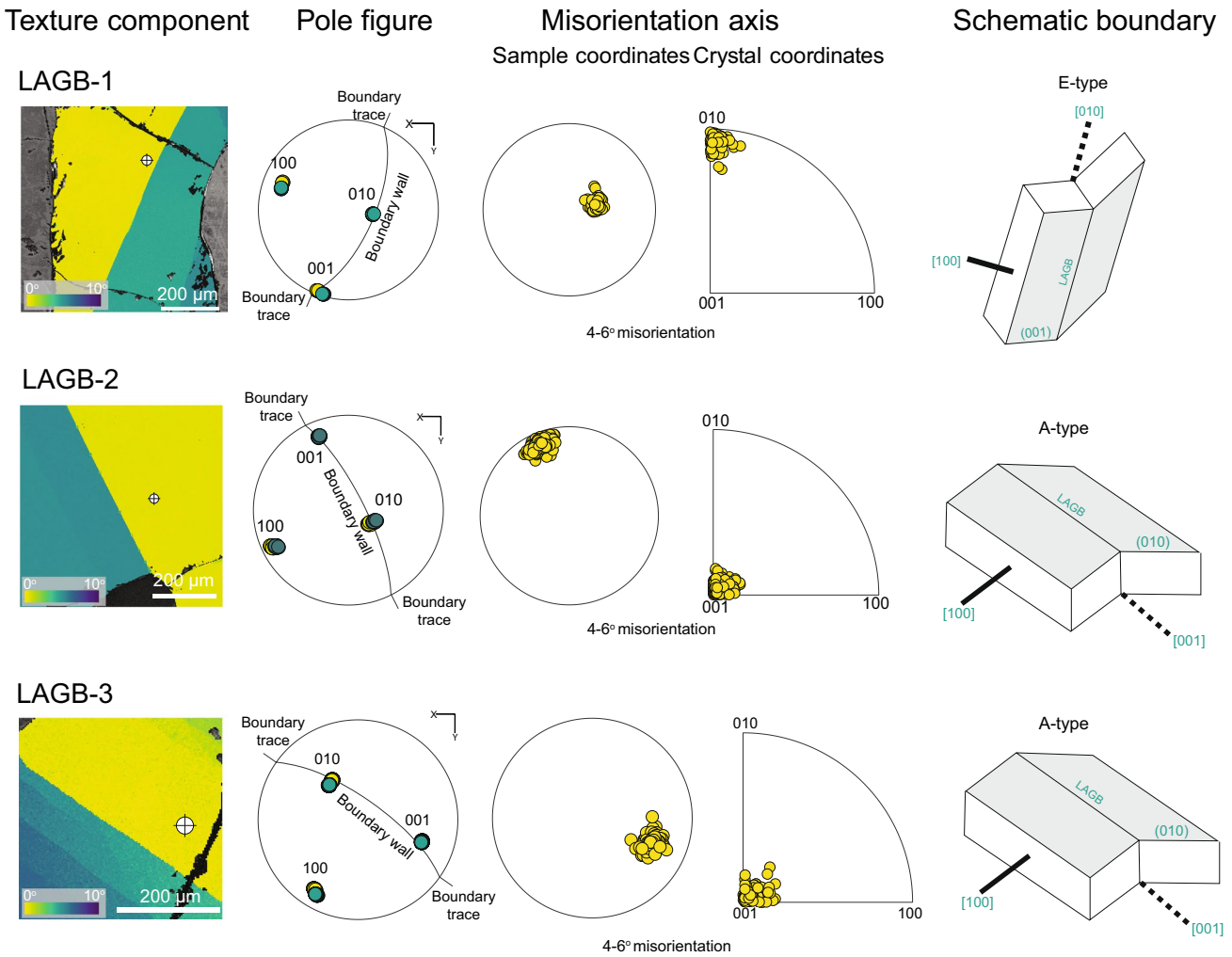

Fig. 2 Analyses of the LAGB-1, -2 and − 3 with EBSD. The first row shows EBSD orientation maps for each grain. Each pixel is colour-coded based on the orientation of a reference point (indicated by the white cross). Pole figures for each LAGB are presented, and the principle crystallographic axes are plotted. The misorientation axes of 4–6° are plotted in sample coordinates in a stereographic plot and crystal coordinates in the orthorhombic fundamental zone The final row depicts a schematic of each grain boundary and the associated slip system. The slip plane is shaded. The misorientation axis is shown with dashed lines, while the slip direction is shown with the solid lines

misorientation axis of [001] direction, likely generated by dislocation slip on the (010) plane in [100] direction.

Two TEM foils per LAGB were taken perpendicular to their respective traces. The foils confirm the boundary plane geometries inferred from the EBSD data and are consistent with the tilt boundary interpretation, based on diffraction patterns and HRTEM micrographs obtained (Fig. 3). LAGB-1 and LAGB-2 show stepped features in their structure. LAGB-1 shows a bigger step, ca. 50 nm, consisting of smaller individual steps ca. 6 nm each (Fig. 3a). The step observed in LAGB-2 is 20 nm with smaller steps ca. 2.5 nm seen within it. In LAGB-2 and LAGB-3 a series of dislocation-associated elastically strained regions of 1.5 nm radius are observed at regular intervals of 5.8 nm and 5.9 nm respectively (Fig. 3d, f). The steep geometry of the misorientation axis in LAGB-1 does not allow for direct observation of the dislocation cores. LAGB-3 exhibits irregularly spaced dislocations at intervals of approximately 165 nm (Fig. 3e, f). Lattice fringes are seen in all three examined LAGB (Fig. 3b, d, f). In LAGB-1 the lattice fringes have a periodic distance of ca. 1 nm. The lattice fringes in LAGB-2 and LAGB-3 are spaced every ca. 0.6 nm. Despite the visible dislocation structure, EDS maps do not show elemental segregation.

Structure and chemistry of LAGBs with APT

Despite the visible dislocation structure in the TEM foils, EDS maps do not show elemental segregation, promoting the use of APT for a detailed analysis of chemical variations. Ten APT specimens were successfully run, two for LAGB-1, five for LAGB-2 and three for LAGB-3. Each

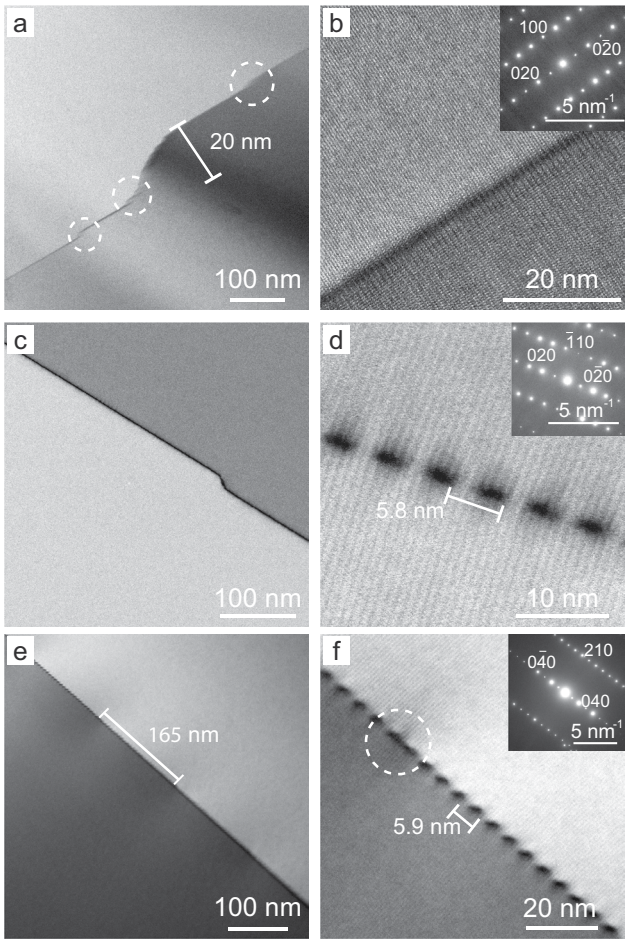

Fig. 3 TEM images of every grain boundary. **a** Overview of LAGB-1, obtained with BF-STEM, showing a 20 nm step and smaller steps, shown in the dashed circles. **b** Close-up, obtained with BF-TEM, of LAGB-1 showing lattice fringes. Also shown the indexed diffraction pattern of the intragrain area close to the boundary. **c** Overview of LAGB-2, obtained with BF-STEM. Also exhibiting a step on its structure. **d** Close-up of LAGB-2, obtained with BF-STEM, showing lattice fringes and regularly spaced dislocation cores. Also shown, the indexed diffraction pattern of the intragrain area close to the boundary. **e** Overview of LAGB-3, obtained with BF-STEM, showing irregular dislocations in constant distances. **f** Close-up of LAGB-3, obtained with BF-STEM, showing lattice fringes and dislocation cores. In the dashed circle a close-up view of one irregularly spaced dislocation. Also shown, the indexed diffraction pattern of the intragrain area close to the boundary

produced 65–100 million counts. The main peaks of the collected mass-to-charge ratio spectra are typical of forsterite major elements and associated ions (e.g. Mg^+, MgO^+, Si^+, SiO^+, O^+, O_2^+) together with smaller peaks for minor (e.g. Fe^+, Ca^+, Al^+, OH^+) and trace elements (e.g. Ti^+, Mn^+, PO^+) (Fig. 4). Both specimens from LAGB-1 successfully captured the targeted grain boundary (Fig. 5a, b), and one specimen each for LAGB-2 and LAGB-3 showed the grain boundary (Fig. 5c, d respectively). The upper parts of the two LAGB-1 APT needles show Ga implantation. These areas have been removed from the reconstructions to avoid artefacts in the elemental analyses. The boundaries are decorated by segregation of minor and trace elements, such as Al, Ca, Fe, H (in the form of OH^-) and Ti, along a plane going through the APT specimens (Fig. 5).

The concentrations of major and minor elements in the intragranular regions were calculated, excluding all grain boundary areas (Table 2). These data are compared with representative olivine compositions previously obtained by electron microprobe analysis (EMPA) for the same sample (Rocco et al. 2012). The APT-derived concentrations are internally consistent across all four specimens. Magnesium ranges between 32.89 and 34.20 at% in APT, compared to 25.2–25.31 at% from EMPA. In contrast, Fe concentrations are lower in APT (1.19–1.29 at%) than in EMPA (3.28–3.37 at%), while Si is higher in APT (17.77–17.88 at%) compared to EMPA (14.15–14.24 at%). Oxygen shows the largest discrepancy, with APT values between 46.07 and 47.76 at% versus 57.14 at% from EMPA. Minor elements Ca, Mn, and Ni show limited variation in APT (0.04, 0.06, and 0.07 at%, respectively) and are broadly comparable to EMPA values (0.02–0.04, 0.03–0.06, and 0.09 at%, respectively).

Concentration differences between the intragranular region and grain boundary concentrations of major elements such as Mg and Si were examined (Fig. 6, S4). The 1D profiles show a slightly reduced Mg in the grain boundaries of all specimens, compared to the intragranular region. Specifically, in LAGB-1a and LAGB 1b, the Mg is reduced from ca. 35 at% to ca. 33 at at%, in LAGB-2 from ca. 34 at% to ca. 33 at% (albeit over a bigger distance) and, finally, in LAGB-3 from ca. 37 at% to ca. 34 at% (Fig. 6). The Si concentrations are relatively similar in LAGB-1a and LAGB-1b (ca. 17.5 at%) compared to the intragranular region, and slightly higher in LAGB-2 and LAGB-3 (up to 18 at% from 17.5 at%) (Fig. 6).

The concentration difference of the minor and trace elements Al, Ca, Fe, H and Ti between the specimens' intragranular region and the LAGBs vary depending on the element (Fig. 6, S4). The concentrations of Al, Ca, Fe and Ti in olivine's intragranular region are comparable between all specimens (ca. 0.1 at%, 0.05 at%, 1.1 at% and 0.02 at% respectively) (Fig. 6). The concentration of Al in the grain boundaries of LAGB-1a, LAGB-1b and LAGB-3 is similar (up to 0.6 at% from 0.1 at%) but is lower for LAGB-2 (ca. 0.4 at%) (Fig. 6). Fe shows a similar trend as Al, with the concentration in LAGB-1a, LAGB-1b and LAGB-3 at a maximum of 1.6 at%, up from 1.1 at%, compared to a more subtle increase in LAGB-2 (from 1.2 at% to 1.3 at%) (Fig. 6). The Ca concentration in LAGB-1a, LAGB-1b and LAGB-2 increases to values of 0.25 at% from 0.05 at%. However, LAGB-3 has a higher Ca concentration of almost 0.5 at% (Fig. 6). The concentration of Ti in LAGB-1a and

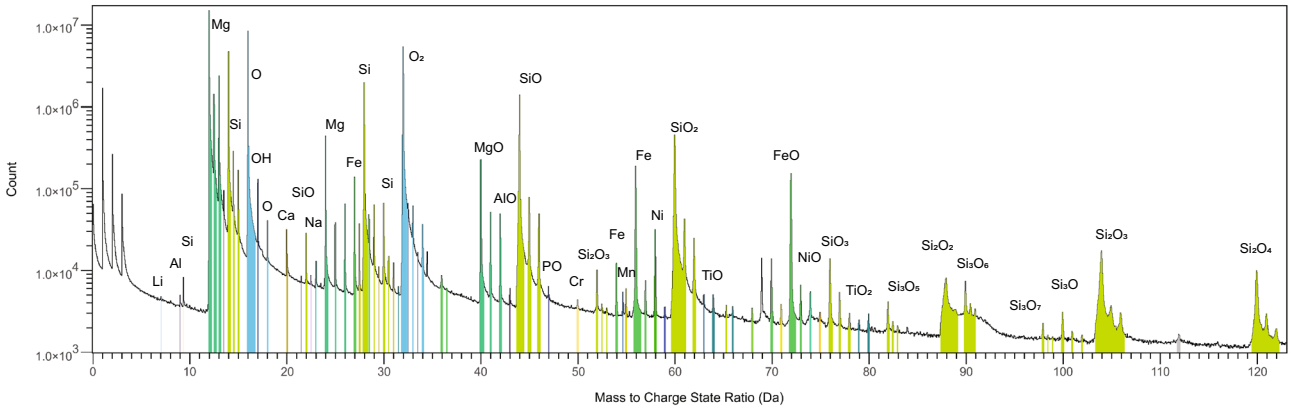

Fig. 4 Example mass-to-charge spectra of the specimen from LAGB-2. The common peaks for olivine are present, as well as smaller peaks for minor and trace elements

LAGB-1b shows an increase to 0.15 at%. The Ti increase in LAGB-2 and LAGB-3 is smaller (up to 0.1 at%) (Fig. 6). The intragranular H concentrations in LAGB-2 and LAGB-3 are similar, at approximately 0.2 at%, with a slight enrichment at the grain boundary (up to ca. 0.3 at%). In contrast, LAGB-1a and LAGB-1b exhibit higher intragranular H concentrations (0.4 and 0.3 at%, respectively) and a more pronounced increase at the grain boundary (reaching up to ca. 0.55 and 0.4 at%, respectively) (Fig. 6).

The calculated interfacial excesses provide a detailed view of elemental segregation while minimizing uncertainties associated with defining grain boundary limits (Felfer et al. 2015; Theska and Primig 2024). The interfacial excesses of minor elements Al, Ca and Fe show different behaviour, dependent on the element (Fig. 7). Al shows broadly similar interfacial excess values in LAGB-1a (0.50 ± 0.00 nm^{-2}), LAGB-1b (0.62 ± 0.04 nm^{-2}), and LAGB-3 (0.66 ± 0.04 nm^{-2}), whereas LAGB-2 exhibits a distinctly lower value (0.35 ± 0.03 nm^{-2}). A comparable pattern is observed for Fe, with excesses of 0.37 ± 0.02 nm^{-2} (LAGB-1a), 0.43 ± 0.02 nm^{-2} (LAGB-1b), and 0.35 ± 0.00 nm^{-2} (LAGB-3), and a lower value in LAGB-2 (0.21 ± 0.01 nm^{-2}). Ca interfacial excess is similar in LAGB-1a, LAGB-1b, and LAGB-2 (0.27 ± 0.04 nm^{-2}, 0.25 ± 0.02 nm^{-2}, and 0.24 ± 0.03 nm^{-2}, respectively). However, LAGB-3 displays an increased excess of 0.42 ± 0.06 nm^{-2}.

Trace elements Ti and H have different interfacial excess behaviour (Fig. 7). Ti exhibits consistent enrichment across all boundaries, with interfacial excess values ranging from 0.08 to 0.10 ± 0.01 nm^{-2}. H enrichment is most pronounced in LAGB-1a (0.14 ± 0.02 nm^{-2}) and LAGB-1b (0.14 ± 0.07 nm^{-2}), while LAGB-2 (0.09 ± 0.05 nm^{-2}) and LAGB-3 (0.04 ± 0.03 nm^{-2}) show comparatively lower values.

The interfacial excess of major elements Mg and Si is, also, shown (Fig. 7). The interfacial excess of Mg in LAGB-1a shows a depletion of 1.68 ± 0.1 nm^{-2}. LAGB-1b shows some variation in Mg, with depletion reported at 2.01 ± 0.05 nm^{-2}. The Mg depletion for LAGB-2 and LAGB-3 is comparable (2.52 ± 0.06 nm^{-2} and 2.44 ± 0.01 nm^{-2} respectively). Si shows limited variation in LAGB-1a and LAGB-1b (-0.18 ± 0.12 nm^{-2} and 0.04 ± 0.04 nm^{-2}, respectively), considering its abundance (ca. 2.5×10^5 cts), while there is a small enrichment in LAGB-2 and LAGB-3 (0.58 ± 0.06 nm^{-2} and 0.62 ± 0.01 nm^{-2} respectively).

Isoconcentration surfaces assist in showing the structure of the grain boundaries in conjunction with 2D profiles (Figs. 5, 8). Specimens LAGB-1a and LAGB-1b appear as planes (Fig. 5a, b). A distinct kinked linear feature is observed in LAGB-1a (Fig. 5a, S5). The 2D profiles show circular features that are regularly spaced and are 4.9 nm apart for LAGB-1a and 4.6 nm apart for LAGB1b (Fig. 8).

Both LAGB-2 and LAGB-3 show similar features to each other (Fig. 5c, d respectively). The grain boundaries comprise a series of parallel lines at regular distances. One of these lines on LAGB-2 and one on LAGB-3 are thicker. The distances of the linear features, measured on the 2D profiles, are 5.7 nm for LAGB-2 and 5.9 nm for LAGB-3 (Fig. 8). Furthermore, LAGB-2 shows an irregularity in the distance of these features (Fig. 8).

Discussion

Olivine grain geochemistry

Olivine geochemistry measured by APT and EMPA shows differences for the grains' major elements. These discrepancies largely reflect known limitations of the APT technique. The O deficiency in olivine APT has been showcased before (Dimitriou et al. 2025), as well as other minerals (e.g. Cappelli et al. 2021). The strong discrepancies in O are, at least

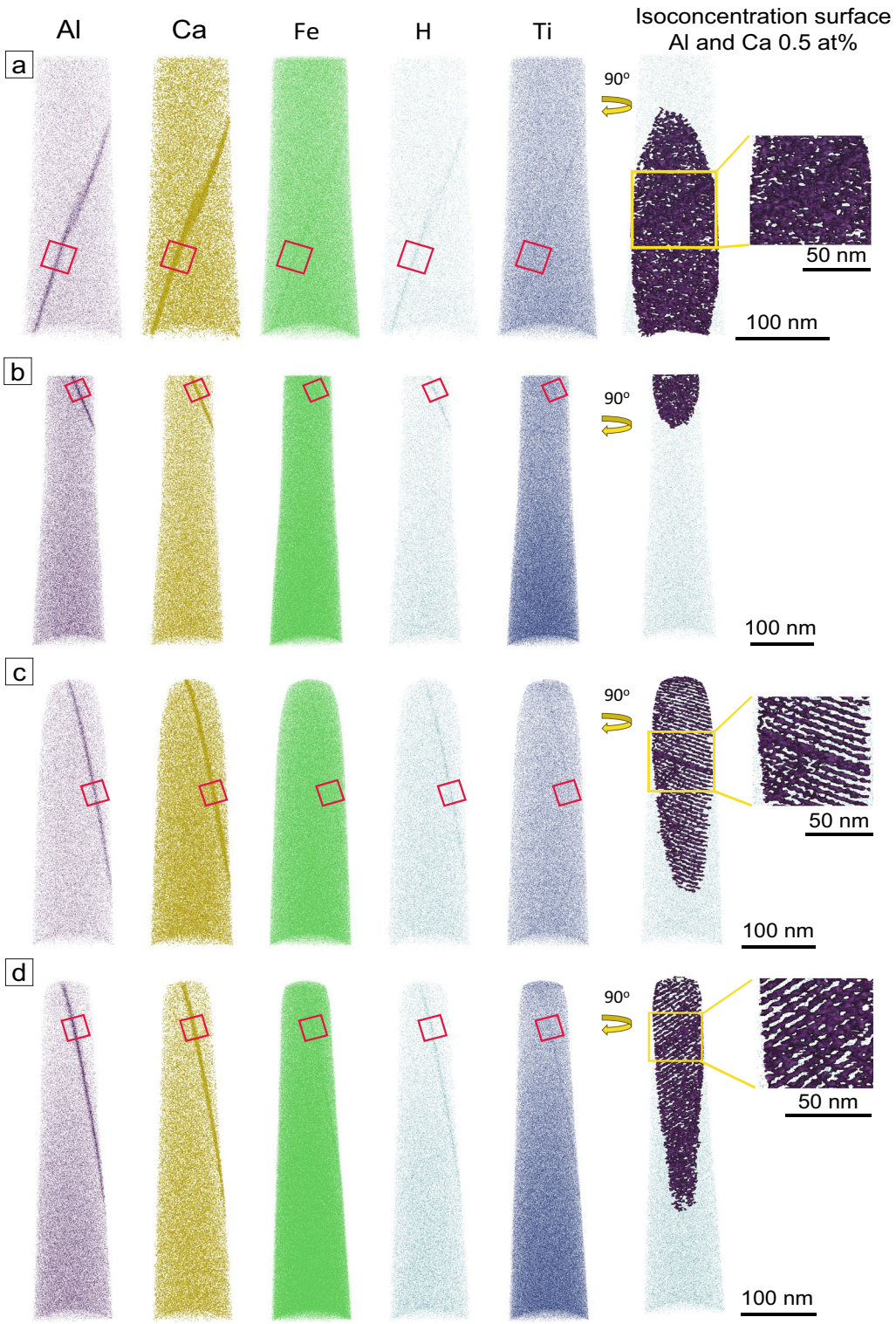

Fig. 5 APT specimen reconstructions displaying elemental maps for Al, Ca, Fe, H and Ti. Isoconcentration surfaces of Al and Ca at 0.5 at% are used to visualise the dislocation cores of the LAGB. Enlarged views of the yellow boxes show spatial modulation in elemental segregation. **(a)** LAGB-1a, **(b)** LAGB-1b, **(c)** LAGB-2, **(d)** LAGB-3. Red boxes show the area, where the 1D profiles were collected from, perpendicularly to the boundaries

Table 2 Major element concentrations (at%) of representative olivine measured by EMPA (Rocco et al. 2012) and of olivine analysed in this study by APT

Sample	Mg	Fe	Si	O	Ca	Mn	Ni	Sum
GF6 (1)	25.31	3.37	14.15	57.14	0.04	0.03	0.09	100.13
GF6 (2)	25.20	3.28	14.24	57.14	0.02	0.06	0.09	100.04
LAGB-1a	34.20	1.26	17.88	46.07	0.03	0.06	0.07	99.57
LAGB-1b	33.86	1.29	17.77	46.50	0.03	0.06	0.08	99.59
LAGB-2	32.89	1.19	17.81	47.76	0.04	0.06	0.07	99.82
LAGB-3	33.62	1.25	17.78	46.79	0.04	0.06	0.07	99.61

partially, responsible for the inaccuracies in the calculated concentrations of the other major elements. Additional errors are produced from peak overlap, e.g. around peaks 28 and 56 between Fe and Si ions. Despite these limitations, minor element concentrations are, overall, in agreement between APT and EMPA. This factor combined with the consistency in the deviations across all specimens support the validity of relative comparisons between grain boundaries' segregation behaviour.

Structural characteristics of the LAGBs

The LAGBs for all studied specimens show no presence of amorphous or different phases, such as melt, different minerals or thin films. Neither the BF-STEM images nor the EBSD data show any evidence of different phases along the grain boundaries (c.f. Montalvo et al. 2019). These observations are consistent with previously reported olivine LAGB structures (e.g. Heinemann et al. 2005; Tacchetto et al. 2021). This is further supported by the APT geochemical data that show major elements concentrations within the typical APT-derived stoichiometry range of olivine (Saxey et al. 2024; Dimitriou et al. 2025).

To interpret the linear features seen in the APT data, we compared their orientation and spacing to the structural evidence obtained from EBSD and TEM. The measured distance between the linear features observed in the APT reconstructions of LAGB-2 and LAGB-3 is almost identical to the distance between the elastically strained regions in the TEM images (Fig. 3d, 3f, 5, 8). This similarity supports the interpretation that the parallel linear features in the APT specimens represent dislocation arrays, similar to the observations in rutile (Verberne et al. 2022) and pyrite (Fougerouse et al. 2024).

For LAGB-1a and LAGB-1b, as the 2D profiles are aligned with the EBSD derived geometry of the main crystallographic axes (Fig. 8), the features observed are parallel to the corresponding misorientation axes (Figs. 2, 8). These geometrical relationships indicate that the features identified correspond to dislocations within the grain boundaries. Moreover, the distance between the dislocations varies from the LAGB-2 and LAGB-3, showcasing the dependence of the internal structure of the grain boundaries on geometry.

Additional defects in the grain boundary structures can be correlated between TEM images and APT reconstructions. The irregularly placed dislocations of LAGB-3, observed in the TEM from the elastically strained region around them, can also be seen in the APT data of LAGB-2 and LAGB-3 (Figs. 3, 5, 8). They appear as "thicker" dislocation arrays in the isoconcentration surfaces in the APT reconstructions. The regular repetition of these steps, every 165 nm, as observed in the TEM, is seen in the APT reconstruction of LAGB-3. A stepped structure similar to the one in TEM foils of LAGB-1 also appear in the APT reconstruction of LAGB-1a (Fig. 5a in the yellow box). All these features are connected with elevated segregation of incompatible elements, shown by the increased thickness of the isoconcentration surfaces around them (Fig. 5) and the increased density of Al (Fig. 8). This highlights the influence of additional defects in the LAGBs' chemistry.

Element partitioning mechanism

The distribution of elements in the LAGBs provides insight into the mechanism responsible for their segregation. Correlative TEM and APT data show that incompatible elements concentrate specifically in the dislocations in the LAGBs, with the areas between them largely retaining the intragrain composition. Furthermore, our TEM and APT data show that there are few to no point defects in the intragrain area. These indicate that incompatible elements accumulated in dislocations that moved to the grain boundary region during upper mantle processes.

The absence of defects in the intragrain regions, coupled with the concentration of incompatible elements within the LAGBs, is consistent with an equilibrium-type segregation process. However, the confinement of solute elements to dislocations cores, rather than being distributed across the entire boundary plane, suggests a dominantly non-equilibrium signature.. When considered into a broader lithospheric context, the rapid ascent and cooling of the xenolith (Rocco et al. 2012) indicate a limited temperature driven re-equilibration. The APT results collectively imply that elemental partitioning at the grain boundary reflects a fast, deformation-related process that was effectively "frozen in" and has remained unmodified since formation.

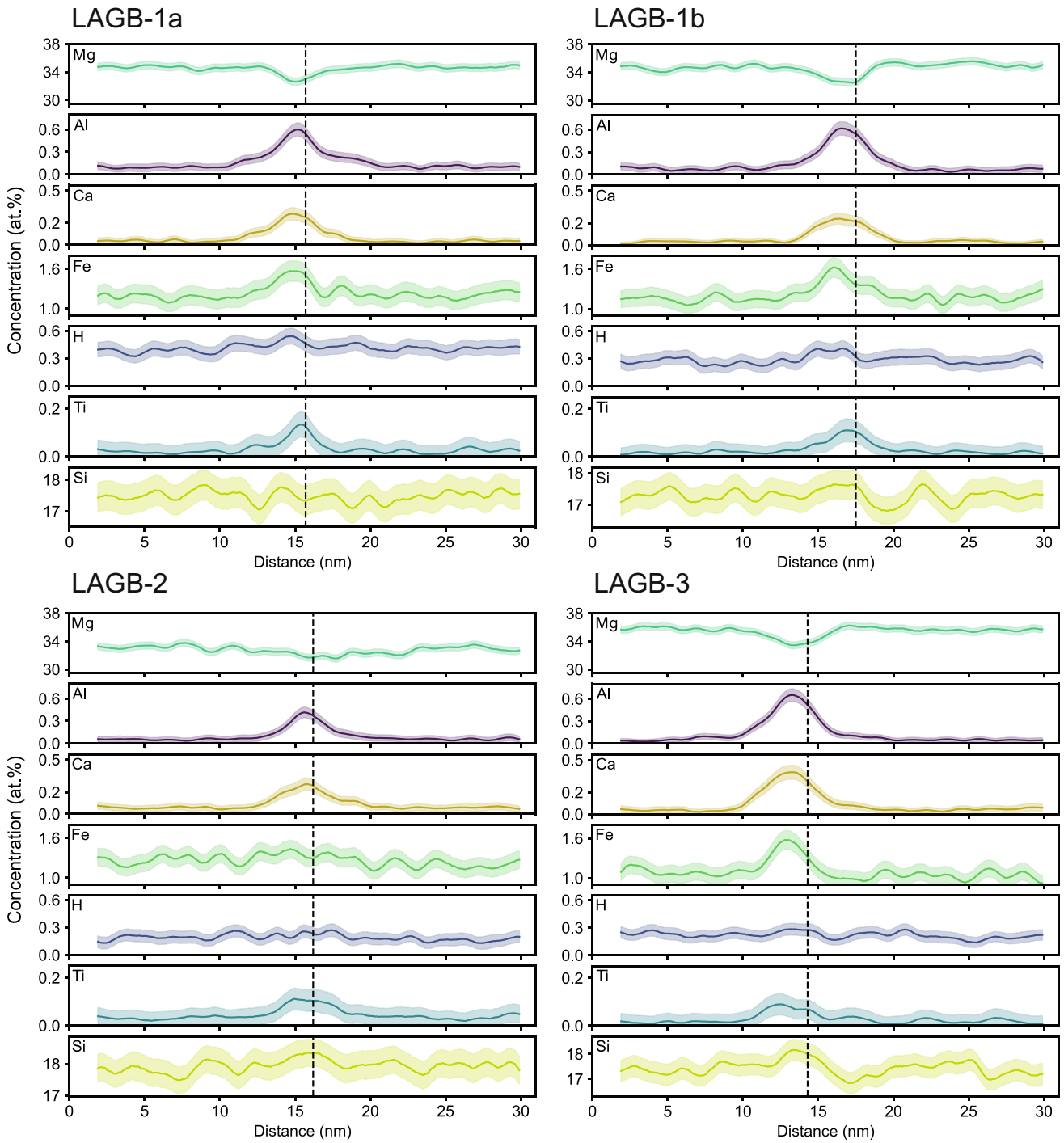

Fig. 6. 1D profiles of major, minor and trace elements Mg, Si, Al, Ca, Fe, H and Ti. The length of the profiles is 30 nm, and they are positioned perpendicular to the LAGBs. The dashed line represents the position of the interface, as calculated by the code by Theska and Primig (2024)

Grain size effect in element segregation in single LAGBs

Minor elements Al, Ca and Fe in LAGB-3 are more strongly segregated to the grain boundary, compared to LAGB-2, despite the same geometry and disorientation angle. More specifically, the enrichment of these elements is almost twice in LAGB-3 compared to LAGB-2 (Fig. 7). This difference could be related, at least partially, to the different sizes of the two grains that the specimens were obtained from (Fig. S3). The grain that LAGB-3 was obtained from has an apparent size twice that of the parent grain of LAGB-2 (ca. 3.03 mm^2 versus 1.52 mm^2). The apparent sizes of the

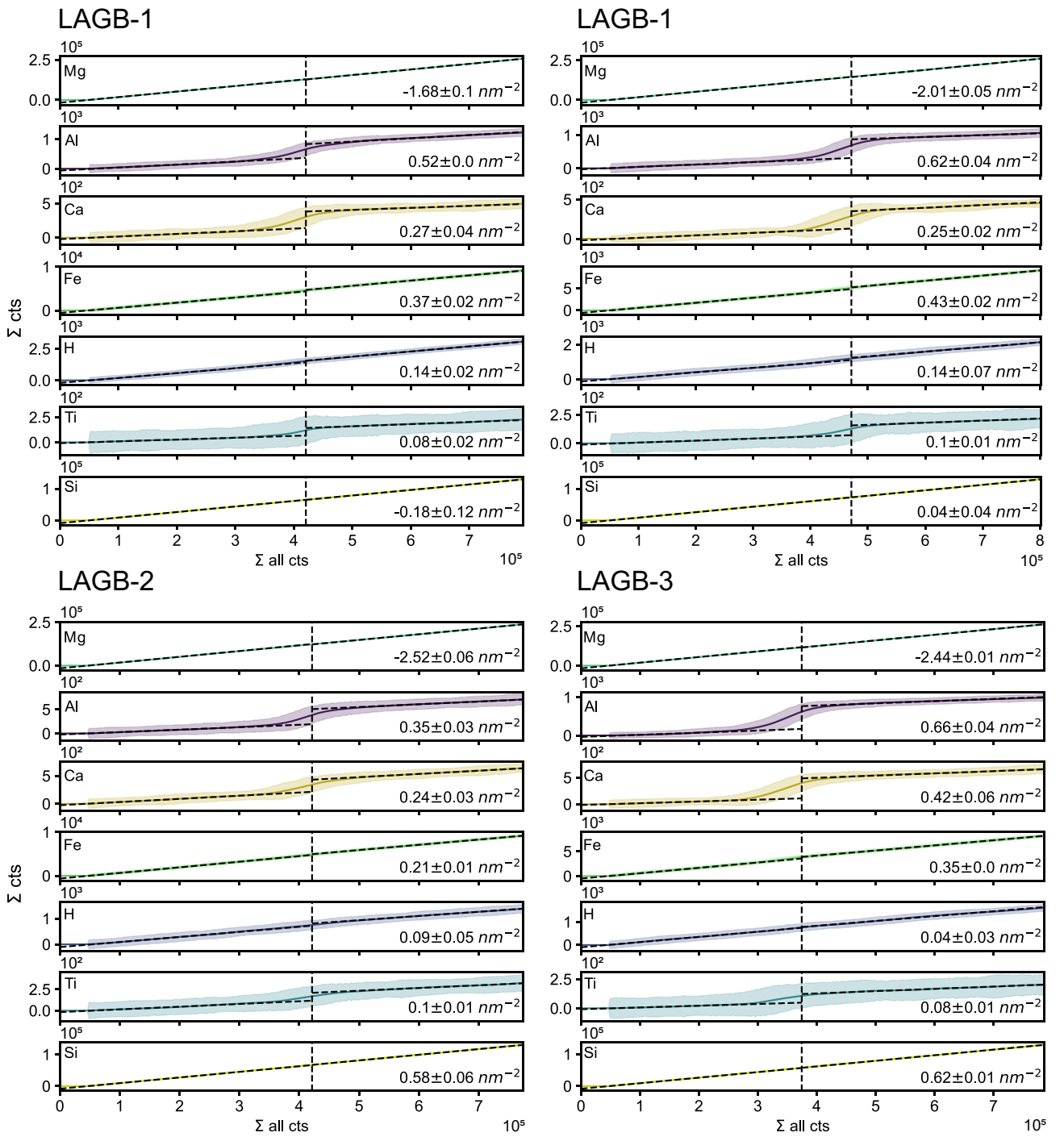

Fig. 7 Interfacial excess plots, derived from the 1D profiles. The plots illustrate the cumulative counts of each examined element as a function of the cumulative counts of all detected elements, calculated in successive increments of 0.1 nm. The plots were created based on the code by Theska and Primig (2024). The dashed line represents the calculated position of the interface. The shaded area displays the error range, propagated from the uncertainties in elemental measurements with APT. The interfacial excess for each element is also displayed

grains of LAGB-1 and LAGB-3 are comparable (3.39 mm^2 and 3.03 mm^2 respectively) (Fig. S3), which could explain the similar minor element segregation observed (with the exception of Ca) (Fig. 7). The correlation between grain size and grain boundary segregation has been reported in material sciences, with the effect being more pronounced with a decrease in grain size and increased abundance of an element (Ishida 1996; Danoix et al. 2022) despite the generally accepted notion that bulk decrease in grain sizes leads to increased concentration of incompatible elements

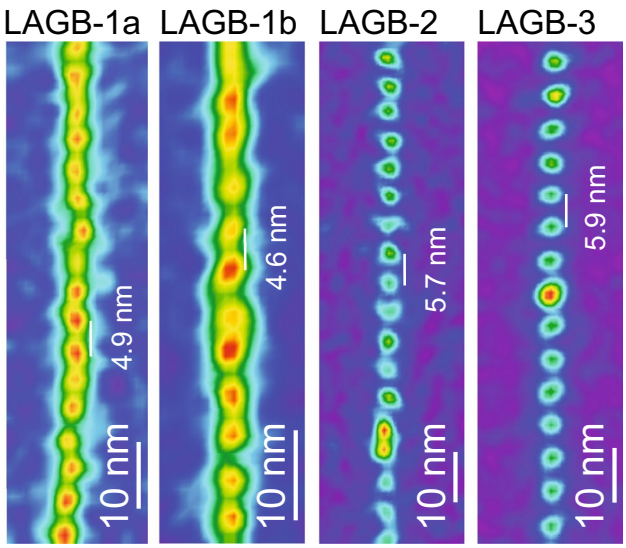

Fig. 8. 2D profiles showing the Al density in the grain boundaries. The orientation of the 2D profiles was determined using the EBSD data

in interfaces (e.g. Hiraga et al. 2007). Our results indicate that grain size likely contributes to the degree of elemental segregation in olivine LAGBs, highlighting a relationship not previously described in geological materials.

Hydrogen segregation in LAGBs

The intragrain measured H concentrations are unusually high ranges for olivine, up to an order of magnitude higher than those previously reported from natural and experimental studies, using FTIR (e.g. Doucet et al. 2014; Padrón-Navarta and Hermann 2017; Zhang et al. 2025). This discrepancy is likely a result of the analytical limitations of APT, particularly the use of 17 Da peak to quantify H, that is affected by overlap with the O at 16 Da, leading to overestimation (Fig. 4). Despite this, experimental studies have shown that olivine can accommodate similar amounts of H, especially at lower upper mantle depths (Bolfan-Casanova et al. 2023). It is, therefore, unclear whether the H concentrations reflect genuine values, differences in sampling scale, or analytical bias. Nevertheless, consistency across specimens here suggest that the relative values and intra-sample trends are robust, even if absolute values should be interpreted with caution.

Fast H diffusivity and resulting fast dehydration of olivine grain have been shown in previous works (Demouchy et al. 2006; Demouchy 2010a). It is not clear from our data whether this is the case here. The concentration of H shows small but meaningful differences through the LAGBs, especially considering the relatively small number of counts. Additionally, the scale of this study only allows to observe the evolution of H concentration over only a few tens of nm compared to previously reported data over several µm. Nevertheless, there is a growing body of evidence supporting that LAGBs experience only limited element exchange after deformation and cooling below a certain threshold (Cherniak and Liang 2014; Tacchetto et al. 2021), supporting that our observations possibly reflect a process that has been essentially frozen.

The segregation of H in natural olivine LAGBs has been demonstrated (Tacchetto et al. 2021). The work here confirms these observations. All grain boundaries show increased segregation of H. Furthermore, H segregation in the (001)[100] LAGBs is increased compared to (010)[100]. This observation shows a connection between boundary geometry and segregation of H. This is, potentially, related to different vacancies created along the grain boundaries, due to the orthorhombic nature of olivine.

A correlation between Ti and H concentration has been hypothesised for olivine grains and grain boundaries (e.g. Berry et al. 2005; Tacchetto et al. 2021; Walker et al. 2007). Our data show that, although there is increased H in the (001)[100] grain, this is not accompanied by an equally increased Ti content (Fig. 6). Furthermore, while segregation of Ti is seen in all of the LAGBs, there is no clear correlation with H segregation in the LAGBs (Fig. S6). The insensitivity of Ti diffusion to crystallography has been described before in bulk olivine (Cherniak and Liang 2014). This shows that the incorporation of H in olivine could be more complex or dependent on other elements apart for Ti. Comparable complexity in H behaviour has been reported before (Walker et al. 2007; Demouchy and Alard 2021; Muir et al. 2022).

The role of Fe in H incorporation has been explored before, associating increased Fe with higher H concentration in experimentally deformed olivine (Katayama and Karato 2008). Our specimens partially reflect this observation, as LAGB-1a and LAGB-1b show higher enrichment of Fe in both the intragrain region and grain boundary, compared to LAGB-2. However, it should be noted that LAGB-3 has similar values of interfacial segregation of Fe to LAGB-1 (Fig. 7). The role of Al could, also, play a pivotal role in H incorporation along the LAGBs, as it creates the charge imbalance necessary. This agrees with our data, as Al follows, overall, the same trends seen in the behaviour of Fe (Figs. 6, 7).

The differences of H concentration in different olivine fabric types have been studied before in experimentally deformed samples (e.g. Jung et al. 2006; Karato et al. 2008; Katayama et al. 2004). These works support higher concentration of H in E-type fabric, commonly associated with (001)[100] slip, compared to A-type fabric, where (010)[100] slip is considered the most dominant. This is confirmed in our data from natural samples, with LAGB-1a and LAGB-1b ((001)[100]) showing increased intragranular H compared to LAGB-2 and LAGB-3 ((010)[100]) (0.3–0.4

at% versus 0.2 at% respectively) (Fig. 6). H incorporation in olivine grains is, hence, complicated and can be associated with both grain boundary segregation and other defects (e.g. point defects).

Major element differences in LAGBs

The behaviour of Mg in LAGBs can be important in understanding dislocation generation. Mg is the main major element that shows depletion in the LAGBs, compared to the relatively consistent to slightly enriched Si along the LAGBs. This shows that the main displacement sites for the generation of dislocations in the crystallographic structure are related to the Mg sites, possibly following previously described models of defect generation related to the M1 and M2 sites in olivine (Wright 2006; Walker et al. 2009; Muir et al. 2020; 2021). The enrichment of Ca against Mg depletion, also, supports the prevalence of M sites' substitutions, behaviour observed before (Hiraga et al. 2004). The depletion of Mg against the increase of concentration of minor and trace elements in the LAGBs show a potential isochemical partition.

The stronger Mg depletion in (010)[100] (LAGB-2 and LAGB-3) shows a potential link between geometry and Mg-related dislocation generation, with (010)[100] boundaries providing a more favourable geometry than (001)[100]. The greater depletion of Mg in LAGB-1b compared to LAGB-1a could be due to the position of the grain boundary at the top of the specimen and the resulting Ga penetration in the grain boundary during FIB preparation, replacing the more abundant species (in this case, Mg). Similar behaviour of Ga replacement in grain boundaries has been reported for Al-alloys, where Ga replaces Al (Unocic et al. 2010).

The Si interfacial excess varies for different boundary types. The relatively stable Si concentration in LAGB-1a and LAGB-1b contrasts with the small enrichment in LAGB-2 and LAGB-3. (Figs. 6, 7). Slight enrichment of Si on olivine LAGBs can also be seen in the data of Tacchetto et al. (2021). These findings contrast with reports of occasional depletion of Si in high-angle grain boundaries relative to the intragranular region (Hiraga et al. 2002). This indicates that the mechanism of elemental segregation on grain boundaries may be different for LAGBs and HAGBs.

Implications for the upper mantle

Segregation of minor and trace elements in LAGBs plays a critical role in upper mantle processes and properties (Tacchetto et al. 2021). The segregation of incompatible elements, such as Al, Ca and H, observed in this work, affects interfacial-controlled and diffusion creep (Mei and Kohlstedt 2000; Yabe et al. 2020; Yabe and Hiraga 2020). This, subsequently, accelerates deformation of the upper mantle. Furthermore, the segregation of H in grain boundaries can accelerate partial melting through the "wetting" of the boundary (Levine et al. 2016). Additionally, H and Fe segregation along grain boundaries, as observed here, can accelerate chemical reactions, such as serpentinization, as these elements are largely responsible for the conversion of olivine into hydrous phases. Finally, the effect of grain boundary diffusion of Mg on the electrical conductivity of the mantle has been explored before with a correlation between increased electrical conductivity and increased Mg vacancies (ten Grotenhuis et al. 2004).

The difference in elemental segregation between the studied slip systems could have far reaching effects on the mantle. Deformation by grain boundary sliding has been found to be accelerated by H in dislocations (Ohuchi et al. 2015). The different H concentration between LAGB types, could, hence, affect deformation, leading to differences in seismic wave attenuation. Finally, increased H in olivine grains has been demonstrated to increase electrical conductivity (Wang et al. 2006; Yoshino et al. 2009). Accordingly, differing H concentration could affect the electrical conductivity of the upper mantle. In addition, the difference in the segregation of Mg between different LAGB geometries, seen in our data, can have an effect on electrical conductivity differences observed in the upper mantle, as Mg vacancies have been related to electric conductivity (ten Grotenhuis et al. 2004).

Conclusions

This study demonstrates that the geometry of olivine tilt LAGBs influences their structure and elemental segregation. LAGBs associated with (010)[100] slip system (associated with A-type fabric) show dislocations in TEM and APT that are ~ 5.8 nm apart. The examined LAGB associated with (001)[100] slip system (most dominant in E-type fabric) has dislocation cores spaced ~ 4.8 nm apart that are only seen with the use of 2D profiles in APT reconstructions. All LAGBs have a stepped structure, as seen in TEM and APT data. Al, Ca, Fe, H and Ti enrichment is seen along the LAGBs, with the effect being more pronounced around the steps. The (001)[100] LAGB shows increased H segregation, whereas (010)[100] LAGBs show greater Mg depletion. The grain size also plays a role in grain boundary elemental segregation; smaller grains, showing (010)[100] LAGBs, are associated with decreased segregation of Al, Ca and Fe.

These compositional variations have implications for upper mantle processes and properties. The increased H segregation connected with (001)[100] LAGBs can accelerate

chemical reactions and phase transitions. At the same time, stronger depletion of Mg in (010)[100] LAGBs could contribute to increased electrical conductivity. Furthermore, the increased Al and Ca in LAGBs increase mantle creep rates. Overall, this study highlights the importance of LAGBs in the behaviour of the upper mantle and provides insight into how variations of their geometry influence upper mantle properties, increasing our understanding of mantle dynamics.

Supplementary Information The online version contains supplementary material available at https://doi.org/10.1007/s00410-026-02318-9.

Acknowledgements We would like to thank Felix Theska for the very useful advice and for providing the modified code that was better suited to our data. We, also, thank Ivana Rocco for providing the sample used here. The authors acknowledge the support of the John de Laeter Centre, Curtin University, whose instrumentation has been supported by funding from the University, State and Commonwealth Government. This study was supported by the Discovery Projects Grant from the Australian Research Council (DP210102625).

Author contributions DD contributed in the conceptualisation of the project, data collection and analysis, original manuscript drafting, reviewing and editing. SMR contributed in a supervisory role, conceptualisation of the project, reviewing and editing, and providing the resources. DF contributed in data validation, reviewing and editing. DWS contributed in data validation, reviewing and editing, and assisted with analysis and data validation. KE contributed in a supervisory role, reviewing and editing, and providing the resources. TT contributed in conceptualisation of the project, reviewing and editing. KM contributed in a supervisory role, reviewing and editing, and assisted with analysis and data validation, and providing the resources.

Funding Open Access funding enabled and organized by CAUL and its Member Institutions

Declarations

Conflicts of interest The authors have no known competing financial interests or personal relationships to declare.

Studies involving humans and/or animals Not applicable.

Ethical approval Not applicable.

References

Adjaoud O, Marquardt K, Jahn S (2012) Atomic structures and energies of grain boundaries in Mg2SiO4 forsterite from atomistic modeling. Phys Chem Miner 39(9):749–760. https://doi.org/10.1007/s00269-012-0529-5

Berry AJ, Hermann J, O'Neill HSC, Foran GJ (2005) Fingerprinting the water site in mantle olivine. Geology 33(11):869–872. https://doi.org/10.1130/G21759.1

Blum TB, Darling JR, Kelly TF, Larson DJ, Moser DE, Perez-Huerta A, Prosa TJ, Reddy SM, Reinhard DA, Saxey DW, Ulfig RM, Valley JW (2018) Best practices for reporting atom probe analysis of geological materials. In: Microstructural Geochronology. American Geophysical Union (AGU) pp 369–373. https://doi.org/10.1002/9781119227250.ch18

Bolfan-Casanova N, Martinek L, Manthilake G, Verdier-Paoletti M, Chauvigne P (2023) Effect of oxygen fugacity on the storage of water in wadsleyite and olivine in H and H-C fluids and implications for melting atop the transition zone. Eur J Mineral 35(4):549–568. https://doi.org/10.5194/ejm-35-549-2023

Bollinger C, Marquardt K, Ferreira F (2019) Intragranular plasticity vs. grain boundary sliding (GBS) in forsterite: microstructural evidence at high pressures (3.5–5.0 GPa). Am Miner 104(2):220–231. https://doi.org/10.2138/am-2019-6629

Cappelli C, Smart S, Stowell H, Pérez-Huerta A (2021) Exploring biases in atom probe tomography compositional analysis of minerals. Geostand Geoanal Res 45(3):457–476. https://doi.org/10.1111/ggr.12395

Carminati EAM, Lustrino M, Cuffaro M, Doglioni C (2010) Tectonics, magmatism and geodynamics of Italy: what we know and what we imagine. https://doi.org/10.3809/jvirtex.2010.00226

Cherniak DJ, Liang Y (2014) Titanium diffusion in olivine. Geochim Cosmochim Acta 147:43–57. https://doi.org/10.1016/j.gca.2014.10.016

Cukjati JT, Cooper RF, Parman SW, Zhao N, Akey AJ, Laiginhas FATP (2019) Differences in chemical thickness of grain and phase boundaries: an atom probe tomography study of experimentally deformed wehrlite. Phys Chem Miner 46(9):845–859. https://doi.org/10.1007/s00269-019-01045-x

Danoix F, Hoummada K, Maugis P, Rolland N, Debreux C, Blavette D (2022) Grain size effect on interfacial segregation in nanomaterials. J Phys Chem Solids 164:110620. https://doi.org/10.1016/j.jpcs.2022.110620

Demouchy S (2010a) Diffusion of hydrogen in olivine grain boundaries and implications for the survival of water-rich zones in the Earth's mantle. Earth Planet Sci Lett 295(1):305–313. https://doi.org/10.1016/j.epsl.2010.04.019

Demouchy S (2010b) Hydrogen diffusion in spinel grain boundaries and consequences for chemical homogenization in hydrous peridotite. Contrib Mineral Petrol 160(6):887–898. https://doi.org/10.1007/s00410-010-0512-4

Demouchy S, Alard O (2021) Hydrogen, trace, and ultra-trace element distribution in natural olivines. Contrib Mineral Petrol 176(4):26. https://doi.org/10.1007/s00410-021-01778-5

Demouchy S, Jacobsen SD, Gaillard F, Stern CR (2006) Rapid magma ascent recorded by water diffusion profiles in mantle olivine. Geology 34(6):429–432. https://doi.org/10.1130/G22386.1

Dimitriou D, Reddy SM, Saxey DW, Fougerouse D, Evans K, Sun X, Rickard WDA (2025) The role of laser pulse energy on data quality and reconstruction of olivine atom probe tomography data. Microsc Microanal 31(3):ozaf040. https://doi.org/10.1093/mam/ozaf040

Dohmen R & Milke R (2010) Diffusion in Polycrystalline Materials: Grain Boundaries, Mathematical Models, and Experimental Data.

Reviews in Mineralogy and Geochemistry 72(1):921–970 https://doi.org/10.2138/rmg.2010.72.21

Doucet LS, Peslier AH, Ionov DA, Brandon AD, Golovin AV, Goncharov AG, Ashchepkov IV (2014) High water contents in the Siberian cratonic mantle linked to metasomatism: an FTIR study of Udachnaya peridotite xenoliths. Geochim Cosmochim Acta 137:159–187. https://doi.org/10.1016/j.gca.2014.04.011

Faul UH, Cline CJ, David EC, Berry AJ, Jackson I (2016) Titanium-hydroxyl defect-controlled rheology of the Earth's upper mantle. Earth Planet Sci Lett 452:227–237. https://doi.org/10.1016/j.epsl.2016.07.016

Felfer P, Scherrer B, Demeulemeester J, Vandervorst W, Cairney JM (2015) Mapping interfacial excess in atom probe data. Ultramicroscopy 159:438–444. https://doi.org/10.1016/j.ultramic.2015.06.002

Ferreira F, Hansen LN, Marquardt K (2021) The effect of grain boundaries on plastic deformation of olivine. J Geophys Res Solid Earth 126(7):e2020JB020273. https://doi.org/10.1029/2020JB020273

Fougerouse D, Reddy SM, Kirkland CL, Saxey DW, Rickard WD, Hough RM (2019) Time-resolved, defect-hosted, trace element mobility in deformed Witwatersrand pyrite. Geosci Front 10(1):55–63. https://doi.org/10.1016/j.gsf.2018.03.010

Fougerouse D, Reddy SM, Aylmore M, Yang L, Guagliardo P, Saxey DW, Rickard WDA, Timms N (2021) A new kind of invisible gold in pyrite hosted in deformation-related dislocations. Geology 49(10):1225–1229. https://doi.org/10.1130/G49028.1

Fougerouse D, Reddy SM, Sumail Brugger J, Thébaud N, Rickard WDA, Yang L, Quadir Z, Roberts MP, Tomkins AG, Martin L, Petrella L, Voisey CR (2024) Dislocation-mediated interfacial re-equilibration of pyrite: an alternative model to interface-coupled dissolution-reprecipitation and gold remobilisation. Geochimica et Cosmochimica Acta 374:136–145. https://doi.org/10.1016/j.gca.2024.04.027

Heinemann S, Wirth R, Gottschalk M, Dresen G (2005) Synthetic [100] tilt grain boundaries in forsterite: 9.9 to 21.5°. Phys Chem Miner 32(4):229–240. https://doi.org/10.1007/s00269-005-0448-9

Hermann J, Fitz Gerald JD, Malaspina N, Berry AJ, Scambelluri M (2007) OH-bearing planar defects in olivine produced by the breakdown of Ti-rich humite minerals from Dabie Shan (China). Contrib Mineral Petrol 153(4):417–428. https://doi.org/10.1007/s00410-006-0155-7

Hiraga T, Anderson I, Zimmerman M, Mei S, Kohlstedt D (2002) Structure and chemistry of grain boundaries in deformed, olivine + basalt and partially molten lherzolite aggregates: evidence of melt-free grain boundaries. Contrib Mineral Petrol 144(2):163–175. https://doi.org/10.1007/s00410-002-0394-1

Hiraga T, Anderson IM, Kohlstedt DL (2004) Grain boundaries as reservoirs of incompatible elements in the Earth's mantle. Nature 427(6976):699–703. https://doi.org/10.1038/nature02259

Hiraga T, Hirschmann MM, Kohlstedt DL (2007) Equilibrium interface segregation in the diopside–forsterite system II: applications of interface enrichment to mantle geochemistry. Geochim Cosmochim Acta 71(5):1281–1289. https://doi.org/10.1016/j.gca.2006.11.020

Hirth JP, Hirth G, Wang J (2020) Disclinations and disconnections in minerals and metals. Proc Natl Acad Sci U S A 117(1):196–204. https://doi.org/10.1073/pnas.1915140117

Humphreys FJ, Bate PS & Hurley PJ (2001) Orientation averaging of electron backscattered diffraction data. Journal of Microscopy 201(1):50–58. https://doi.org/10.1046/j.1365-2818.2001.00777.x

Ishida K (1996) Effect of grain size on grain boundary segregation. J Alloys Compd 235(2):244–249. https://doi.org/10.1016/0925-8388(95)02094-2

Jung H, Katayama I, Jiang Z, Hiraga T, Karato S (2006) Effect of water and stress on the lattice-preferred orientation of olivine. Tectonophysics 421(1):1–22. https://doi.org/10.1016/j.tecto.2006.02.011

Karato S, Jung H, Katayama I & Skemer P (2008) Geodynamic significance of seismic anisotropy of the upper mantle: New insights from laboratory studies. Annual Review of Earth and Planetary Sciences 36(1):59–95

Katayama I, Karato S-I (2008) Effects of water and iron content on the rheological contrast between garnet and olivine. Phys Earth Planet Inter 166(1):57–66. https://doi.org/10.1016/j.pepi.2007.10.004

Katayama I, Jung H, Karato S (2004) New type of olivine fabric from deformation experiments at modest water content and low stress. Geology 32(12):1045–1048. https://doi.org/10.1130/G20805.1

Khisina NR, Wirth R (2002) Hydrous olivine (Mg1−yFe2+y)2−xvxSiO4H2x– a new DHMS phase of variable composition observed as nanometer-sized precipitations in mantle olivine. Phys Chem Miner 29(2):98–111. https://doi.org/10.1007/s002690100205

Khisina N, Wirth R, Matsyuk S, Koch-Müller M (2008) Microstructures and OH-bearing nano-inclusions in "wet" olivine xenocrysts from the Udachnaya kimberlite. Eur J Mineral 20(6):1067–1078. https://doi.org/10.1127/0935-1221/2008/0020-1799

Kitamura M, Kondoh S, Morimoto N, Miller GH, Rossman GR, Putnis A (1987) Planar OH-bearing defects in mantle olivine. Nature 328(6126):143–145. https://doi.org/10.1038/328143a0

Levine JSF, Mosher S, Rahl JM (2016) The role of subgrain boundaries in partial melting. J Struct Geol 89:181–196. https://doi.org/10.1016/j.jsg.2016.06.006

Lloyd GE, Farmer AB, Mainprice D (1997) Misorientation analysis and the formation and orientation of subgrain and grain boundaries. Tectonophysics 279(1):55–78. https://doi.org/10.1016/S0040-1951(97)00115-7

Lloyd GE, Lee AL, Kahl M (2021) A practical method to determine the five-parameter orientation of intragranular boundaries in polycrystals. Tectonophysics 814:228955. https://doi.org/10.1016/j.tecto.2021.228955

Lustrino M, Melluso L, Morra V (2000) The role of lower continental crust and lithospheric mantle in the genesis of Plio-Pleistocene volcanic rocks from Sardinia (Italy). Earth Planet Sci Lett 180(3):259–270. https://doi.org/10.1016/S0012-821X(00)00185-0

Lustrino M, Morra V, Melluso L, Brotzu P, Damelio F, Fedele L, Franciosi L, Lonis R, Petteruti Liebercknekt AM (2004) The cenozoic igneous activity of sardinia. https://iris.uniroma1.it/handle/11573/37648 [2025–03–06]

Lustrino M, Morra V, Fedele L, Serracino M (2007) The transition between 'orogenic' and 'anorogenic' magmatism in the western Mediterranean area: the Middle Miocene volcanic rocks of Isola del Toro (SW Sardinia, Italy). Terra Nova 19(2):148–159. https://doi.org/10.1111/j.1365-3121.2007.00730.x

Lustrino M, Fedele L, Melluso L, Morra V, Ronga F, Geldmacher J, Duggen S, Agostini S, Cucciniello C, Franciosi L, Meisel T (2013) Origin and evolution of Cenozoic magmatism of Sardinia (Italy). A combined isotopic (Sr–Nd–Pb–O–Hf–Os) and petrological view. Lithos 180–181:138–158. https://doi.org/10.1016/j.lithos.2013.08.022

Mainprice D, Tommasi A, Couvy H, Cordier P, Frost DJ (2005) Pressure sensitivity of olivine slip systems and seismic anisotropy of Earth's upper mantle. Nature 433(7027):731–733. https://doi.org/10.1038/nature03266

Marquardt K, Faul UH (2018) The structure and composition of olivine grain boundaries: 40 years of studies, status and current developments. Phys Chem Miner 45(2):139–172. https://doi.org/10.1007/s00269-017-0935-9

Marquardt K, Rohrer GS, Morales L, Rybacki E, Marquardt H, Lin B (2015) The most frequent interfaces in olivine aggregates: the GBCD and its importance for grain boundary related processes.

Contrib Mineral Petrol 170(4):40. https://doi.org/10.1007/s00410-015-1193-9
Mei S, Kohlstedt DL (2000) Influence of water on plastic deformation of olivine aggregates: 2. Dislocation creep regime. J Geophys Res Solid Earth 105(B9):21471–21481. https://doi.org/10.1029/2000JB900180
Miyake M, Nakamura H, Kojima H & Marumo F (1987) Cation ordering in Co-Mg olivine solid-solution series. American Mineralogist 72(5–6):594–598
Montalvo SD, Reddy SM, Saxey DW, Rickard WDA, Fougerouse D, Quadir Z, Johnson TE (2019) Nanoscale constraints on the shock-induced transformation of zircon to reidite. Chem Geol 507:85–95. https://doi.org/10.1016/j.chemgeo.2018.12.039
Muir JMR, Jollands M, Zhang F, Walker AM (2020) Explaining the dependence of M-site diffusion in forsterite on silica activity: a density functional theory approach. Phys Chem Miner 47(12):55. https://doi.org/10.1007/s00269-020-01123-5
Muir JMR, Zhang F, Walker AM (2021) The mechanism of Mg diffusion in forsterite and the controls on its anisotropy. Phys Earth Planet Inter 321:106805. https://doi.org/10.1016/j.pepi.2021.106805
Muir JMR, Jollands M, Zhang F, Walker AM (2022) Controls on the distribution of hydrous defects in forsterite from a thermodynamic model. Phys Chem Miner 49(4):7. https://doi.org/10.1007/s00269-022-01182-w
Ohuchi T, Kawazoe T, Higo Y, Funakoshi K, Suzuki A, Kikegawa T & Irifune T (2015) Dislocation-accommodated grain boundary sliding as the major deformation mechanism of olivine in the Earth's upper mantle. Science Advances 1(9):e1500360. https://doi.org/10.1126/sciadv.1500360
Overwijk MHF, van den Heuvel FC, Bulle-Lieuwma CWT (1993) Novel scheme for the preparation of transmission electron microscopy specimens with a focused ion beam. J Vac Sci Technol B Microelectron Nanometer Struct Process Meas Phenom 11(6):2021–2024. https://doi.org/10.1116/1.586537
Padrón-Navarta JA, Hermann J (2017) A subsolidus olivine water solubility equation for the Earth's upper mantle. J Geophys Res Solid Earth 122(12):9862–9880. https://doi.org/10.1002/2017JB014510
Peccerillo A (2017) Cenozoic volcanism in the tyrrhenian Sea Region. In: Cenozoic Volcanism in the Tyrrhenian Sea Region. https://doi.org/10.1007/978-3-319-42491-0
Piazolo S, La Fontaine A, Trimby P, Harley S, Yang L, Armstrong R, Cairney JM (2016) Deformation-induced trace element redistribution in zircon revealed using atom probe tomography. Nat Commun 7(1):10490
Putnis A, John T (2010) Replacement processes in the Earth's crust. Elements 6(3):159–164. https://doi.org/10.2113/gselements.6.3.159
Raterron P, Chen J, Li L, Weidner D, Cordier P (2007) Pressure-induced slip-system transition in forsterite: single-crystal rheological properties at mantle pressure and temperature. Am Mineral 92(8–9):1436–1445. https://doi.org/10.2138/am.2007.2474
Reddy SM, Timms NE, Pantleon W, Trimby P (2007) Quantitative characterization of plastic deformation of zircon and geological implications. Contrib Mineral Petrol 153(6):625–645. https://doi.org/10.1007/s00410-006-0174-4
Reddy SM, Saxey DW, Rickard WDA, Fougerouse D, Montalvo SD, Verberne R, van Riessen A (2020) Atom probe tomography: development and application to the geosciences. Geostand Geoanal Res 44(1):5–50. https://doi.org/10.1111/ggr.12313
Rickard WDA, Reddy SM, Saxey DW, Fougerouse D, Timms NE, Daly L, Peterman E, Cavosie AJ, Jourdan F (2020) Novel applications of FIB-SEM-based ToF-SIMS in atom probe tomography workflows. Microsc Microanal 26(4):750–757. https://doi.org/10.1017/S1431927620000136
Rocco I, Lustrino M, Morra V, Melluso L (2012) Petrological, geochemical and isotopic characteristics of the lithospheric mantle beneath Sardinia (Italy) as indicated by ultramafic xenoliths enclosed in alkaline lavas. Int J Earth Sci 101(5):1111–1125. https://doi.org/10.1007/s00531-011-0729-0
Saxey DW, Fougerouse D, Dimitriou D, Barnes JJ, Rickard WDA, Timms NE, Jourdan F, Reddy SM, Bland PA, Ireland TR, Nguyen A, Connolly HC Jr., Lauretta DS (2024) Geochemical quantification of olivine minerals by atom probe tomography. Microsc Microanal 30(Supplement_1):ozae044.032. https://doi.org/10.1093/mam/ozae044.032
Schaffer M, Schaffer B, Ramasse Q, Falke M, Abou-Ras D, Schmidt S, Caballero R, Marquardt K (2011) Optimized FIB sample preparation for atomic resolution analytical STEM at low kV - a key requirement for successful application. Microsc Microanal 17(S2):630–631. https://doi.org/10.1017/S1431927611004028
Skemer P, Hansen LN (2016) Inferring upper-mantle flow from seismic anisotropy: an experimental perspective. Tectonophysics 668–669:1–14. https://doi.org/10.1016/j.tecto.2015.12.003
Sommer H, Regenauer-Lieb K, Gasharova B, Siret D (2008) Grain boundaries: a possible water reservoir in the Earth's mantle? Mineral Petrol 94(1):1–8. https://doi.org/10.1007/s00710-008-0002-9
Tacchetto T, Reddy SM, Saxey DW, Fougerouse D, Rickard WDA, Clark C (2021) Disorientation control on trace element segregation in fluid-affected low-angle boundaries in olivine. Contrib Mineral Petrol 176(7):59. https://doi.org/10.1007/s00410-021-01815-3
ten Grotenhuis SM, Drury MR, Peach CJ, Spiers CJ (2004) Electrical properties of fine-grained olivine: Evidence for grain boundary transport. Journal of Geophysical Research: Solid Earth. https://doi.org/10.1029/2003JB002799
Theska F, Primig S (2024) Interfacial excess of solutes across phase boundaries using atom probe microscopy. Ultramicroscopy 256:113885. https://doi.org/10.1016/j.ultramic.2023.113885
Thompson K, Lawrence D, Larson DJ, Olson JD, Kelly TF & Gorman B (2007) In situ site-specific specimen preparation for atom probe tomography. Ultramicroscopy 107(2):131–139. https://doi.org/10.1016/j.ultramic.2006.06.008
Unocic K, Mills M, Daehn G (2010) Effect of gallium focused ion beam milling on preparation of aluminium thin foils. J Microsc 240(3):227–238. https://doi.org/10.1111/j.1365-2818.2010.03401.x
Verberne R, Reddy SM, Saxey DW, Fougerouse D, Rickard WDA, Quadir Z, Evans NJ, Clark C (2022) Dislocations in minerals: fast-diffusion pathways or trace-element traps? Earth Planet Sci Lett 584:117517. https://doi.org/10.1016/j.epsl.2022.117517
Wagner J, Adjaoud O, Marquardt K & Jahn S (2016) Anisotropy of self-diffusion in forsterite grain boundaries derived from molecular dynamics simulations. Contributions to Mineralogy and Petrology 171(12):98. https://doi.org/10.1007/s00410-016-1308-y
Walker AM, Woodley SM, Slater B, Wright K (2009) A computational study of magnesium point defects and diffusion in forsterite. Phys Earth Planet Inter 172(1):20–27. https://doi.org/10.1016/j.pepi.2008.04.001
Walker AM, Hermann J, Berry AJ, O'Neill HSC (2007) Three water sites in upper mantle olivine and the role of titanium in the water weakening mechanism. J Geophys Res Solid Earth 112(B5). https://doi.org/10.1029/2006JB004620
Wang D, Mookherjee M, Xu Y & Karato S (2006) The effect of water on the electrical conductivity of olivine. Nature 443(7114):977–980. https://doi.org/10.1038/nature05256
Wright K (2006) Atomistic models of OH defects in nominally anhydrous minerals. Rev Mineral Geochem 62(1):67–83. https://doi.org/10.2138/rmg.2006.62.4

Xie D, Hirth G, Hirth JP, Wang J (2019) Defects in deformation twins in plagioclase. Phys Chem Miner 46(10):959–975. https://doi.org/10.1007/s00269-019-01055-9

Yabe K, Hiraga T (2020) Grain-boundary diffusion creep of olivine: 2. Solidus effects and consequences for the viscosity of the oceanic upper mantle. J Geophys Res Solid Earth 125(8):e2020JB019416. https://doi.org/10.1029/2020JB019416

Yabe K, Sueyoshi K, Hiraga T (2020) Grain-Boundary Diffusion Creep of Olivine: 1. Experiments at 1 atm. J Geophys Res Solid Earth 125(8):e2020JB019415. https://doi.org/10.1029/2020JB019415

Yoshino T, Matsuzaki T, Shatskiy A & Katsura T (2009) The effect of water on the electrical conductivity of olivine aggregates and its implications for the electrical structure of the upper mantle. Earth and Planetary Science Letters 288(1):291–300 https://doi.org/10.1016/j.epsl.2009.09.032

Zhang K, Li L, Stern CR, Yang X (2025) Water solubility of olivine under redox-controlled deep upper mantle conditions: effects of pressure, temperature and coexisting fluids and implications. Contrib Mineral Petrol 180(1):9. https://doi.org/10.1007/s00410-024-02197-y